Local atomic structures and lattice dynamics of inverse colossal barocaloric ammonium thiocyanate

Zhe Zhang[1,2] Wu Gong,[3] Xueting Zhao[1,2] Ji Qi,[1,2] Mingze Li[1,2] Shuki Torii,[4] Huaican Chen,[5,6]
Wen Yin,[5,6] Koji Ohara,[7] Zhidong Zhang[1,2] Yukinobu Kawakita,[3,*] and Bing Li[1,2,*]

[1]*Shenyang National Laboratory for Materials Science, Institute of Metal Research,*
Chinese Academy of Sciences, 72 Wenhua Road, Shenyang, Liaoning 110016, China
[2]*School of Materials Science and Engineering, University of Science and Technology of China, 72 Wenhua Road,*
Shenyang, Liaoning 110016, China
[3]*J-PARC Center, Japan Atomic Energy Agency, Tokai, Ibaraki 319-1195, Japan*
[4]*Institute of Materials Structure Science, High Energy Accelerator Research Organization, Tokai, Ibaraki, 319-1106, Japan*
[5]*Institute of High Energy Physics, Chinese Academy of Sciences, Beijing 100049, China*
[6]*Spallation Neutron Source Science Center, Dongguan 523803, China*
[7]*SPring-8, Diffraction and Scattering Division, Japan Synchrotron Radiation Research Institute, 1-1-1 Kouto,*
Sayo-Cho, Sayo-Gun, Hyogo 679-5198, Japan

NH_4SCN exhibits successive phase transitions from monoclinic to orthorhombic, and then to tetragonal. The former phase transition is accompanied by an inverse colossal barocaloric effect and a huge negative thermal expansion. This transition is complicated by the possibly coexisting orientational disorder of NH_4^+ and SCN^-, and the mechanism is still unclear. Here, NH_4SCN is investigated using high-resolution neutron powder diffraction, pair distribution function analysis, and Raman scattering. Both the average and local structural analyses indicate that only NH_4^+ is orientationally disordered in the orthorhombic phase, and SCN^- becomes subsequently disordered in the tetragonal phase. Both temperature-induced and pressure-induced hardening behaviors of SCN^--related vibrations are observed, which lead to the breakage of hydrogen bonds-linked NH_4^+ with SCN^- and further facilitate phase transition. Our findings provide a solid standing point of atomic structures and dynamics on which the scenario of the phase transition and the associated physical properties are established.

I. INTRODUCTION

Caloric effects, referred to as thermal effects of phase transitions induced by a specific external field in solid materials, provide a promising solution to emission-free refrigeration technology. The discovery of colossal barocaloric effects (BCEs) of plastic crystals opens an emerging pathway to this goal, thanks to their ten times higher entropy changes and significantly reduced driving pressures compared to previous materials [1–6]. Plastic crystals—a kind of soft, solid material—are characteristic of orientation-ordered to orientation-disordered solid-state phase transitions, which are easily driven by hydrostatic pressure [7]. Through this transition, plastic crystals will retain their translational symmetry while losing orientational orders, liberating considerably latent heat comparable to the enthalpy of fusion [8–10]. Most of the reported barocaloric materials exhibit so-called normal BCEs, appearing as heating at pressurization and cooling at depressurization during the solid-state refrigeration cycle. Conversely, there is an inverse BCE with cooling at pressurization and heating at depressurization. So far, there are only very few materials that exhibit inverse BCEs.

NH_4SCN is an ionic plastic crystal material and undergoes successive phase transitions from monoclinic to orthorhombic at 360 K, and to tetragonal at 390 K [11–17], which correspond to low-temperature, medium-temperature, and high-temperature phases, respectively. NH_4SCN was reported to be the first inverse barocaloric material, with entropy changes higher than $100\,\mathrm{J\,kg^{-1}\,K^{-1}}$, associated with the low-temperature phase transition. Around 360 K, the maximum isothermal entropy change of $128.7 \pm 4.4\,\mathrm{J\,kg^{-1}\,K^{-1}}$ was obtained under an applied hydrostatic pressure P of 80 MPa. Moreover, it is unique that both a large entropy change and large relative cooling power were simultaneously achieved in this material, which is usually inversely related [11]. In addition to the regular refrigeration application, barocaloric thermal storage was proposed and realized in NH_4SCN as well, based on the inverse BCE. The thermal hysteresis of the transition is about 29 K, which is unfavorable for refrigeration applications but advantageous for thermal storage. This is because, under a specific pressure, a greater thermal hysteresis leads to a broader operating temperature range. In this scheme, thermal charging is initialized upon pressurization through the plastic crystal transition, and the discharging of $43\,\mathrm{J\,g^{-1}}$ takes place at depressurization, which is 11 times more than the input mechanical energy [11].

Despite excellent and unique barocaloric properties, the mechanism of the underlying phase transition remains

---

*bingli@imr.ac.cn, and yukinobu.kawakita@j-parc.jp

unclear. There is a debate about the ordering or not of SCN^- in the structure of the orthorhombic phase. In previous experiments of polarized Raman scattering [18], both SCN^- and NH_4^+ were found to be disordered in the orthorhombic phase. In contrast, neutron powder diffraction and single-crystal x-ray diffraction analysis suggest that SCN^- ions were ordered while NH_4^+ ions were disordered [12–14]. In molecular dynamics simulations, the inverse BCE was ascribed to the pressure-enhanced transverse vibrations of SCN^- and the pressure-suppressed hydrogen bonding between NH_4^+ and SCN^- ions [11]. The pressure-enhanced disorder was indeed observed in quasielastic neutron scattering, while the detailed roles of atomic vibrations are still unknown. In this work, we ascertain the crystal structure of each phase with the support of high-resolution neutron diffraction spectra and determine the ordered state of SCN^- in the orthorhombic phase. Local atomic structures determined by pair distribution function (PDF) analysis indicate that the peak positions representing intermolecular atomic pairs shift to a lower distance r after plastic crystal transition is caused by lattice contraction, and the accompanying broadening is mainly caused by the enhanced orientational disordering. Furthermore, pressure-dependent atomic vibrational modes investigated using Raman scattering suggest that pressure leads to significant hardening of SCN^--related vibrations, especially the translational modes.

II. EXPERIMENTAL METHODS

High-quality, colorless ND_4SCN (99.27 atom% deuterium) and NH_4SCN powders (purity: 99.99%) were purchased from Santa Cruz Biotechnology and Aladdin, respectively. The high-resolution neutron powder diffraction experiments were conducted on ND_4SCN at varying temperatures at the Super High-Resolution Powder Diffractometer (SuperHRPD) of J-PARC in Japan [19]. A Pt-100 sensor was used for temperature calibration. The resolution $\Delta d/d$ can reach $\sim$0.035%, which allows us to distinguish a tiny change in crystal structures. The temperature range of the measurements was from 300 to 400 K, with an interval of 10 K. At 300, 370, and 400 K, where the compound crystallizes in three distinct phases, long scans of up to 6 h were taken to obtain high-quality data for detailed structural refinements. At other temperatures, the acquisition time was 3 h. To ensure a homogenous temperature of the sample, a waiting time of 1400 s was allowed when reaching a given temperature. The obtained data were analyzed using the Rietveld refinement method in the Z-Rietveld software [20]. The neutron total scattering of ND_4SCN was carried out using the multiphysics instrument (MPI) of the China Spallation Neutron Source (CSNS) in China [21]. A deuterated powder sample with a mass of 1.029 g was loaded into a cylindrical vanadium container ($\phi = 9.51$ mm, $L = 75.2$ mm). A K-type thermocouple was used for measurements. Constant temperature scans were performed at 300, 380, and 400 K in the heating process, respectively, where the duration at each temperature was 10 h. The total scattering data were reduced using Mantid software [22], which corrected, normalized, and collated the information from the seven banks. The absorption correction and multiple scattering correction were applied. An empty can

was measured for background subtraction. The normalized structural factor $S(Q)$ was Fourier-transformed to generate the PDF, $G(r)$, with a cutoff of 50 Å^{-1}. The PDF analysis was implemented using PDFgui software based on the monoclinic structural model [23]. The refined parameters include lattice parameters, atomic position, scale factors, and delta, and the Q damping was confined to 0.1. The fitting r range was 0.6 to 13 Å. The atomic structures were visualized in VESTA software [24].

The temperature- and pressure-dependent Raman scattering spectra of NH_4SCN were collected using a commercial Raman spectrometer (LabRAM HR Evolution, HORIBA Jobin Yvon) with the ultralow frequency mode. The wavelength of the laser was 633 nm. The temperature and the high-pressure environments were realized using a symmetric diamond anvil cell (Diacell® cryoDAC-Tesla, Almax easyLab) and an accommodating cryofurnace. The applied pressures were calibrated using the ruby fluorescence method. Two Pt-100 sensors were utilized for temperature calibration. Constant temperature and pressure scans were performed in the conditions of wave numbers from 5 to 250 cm^{-1}, temperatures from 300 to 390 K, and P from 0.1 to 1110 MPa. These pressures are not adequately precise due to the unavoidable error in the low-pressure range. Under a given condition, a few minutes were allowed for equilibration before counting. All acquired Raman scattering spectra were processed by LabSpec6 software. The Raman profiles were fitted to a combination of multiple Lorentzian functions to determine the peak position of an individual peak.

III. RESULTS AND DISCUSSION

A. Average crystal structures

It is well known that there are three crystallographic phases in NH_4SCN—monoclinic (space group $P2_1/c$), orthorhombic (space group $Pbcm$), and tetragonal (space group $I4/mcm$)—temperature rises [12–17]. While the full structural information of the monoclinic phase is readily available, the atomic coordinates in the other two phases are not well determined due to the existence of the orientational disorder. Taking into account the imperfect deuterated quality of the sample and the limited resolution of the diffraction spectrometer in past research [11], the results cannot resolve the controversy of SCN^-. Here, we systematically revisit the crystal structures using a fully deuterated sample with a high-resolution diffractometer.

Figure 1(a)–1(c) shows the diffraction patterns and their refinements at 300, 370, and 400 K, respectively. At higher temperatures, one can see fewer Bragg peaks, indicating the elevated lattice symmetry. In addition, the intensities of the Bragg peaks are reduced, owing to the activated molecular orientational disorder [25,26]. These diffraction patterns are fitted to a few different models. The pattern at 300 K is well reproduced by the $P2_1/c$ model with both ordered ND_4^+ and SCN^- ions, which is consistent with previous reports [11–14]. As for the data collected at 370 K, both the ordered and disordered SCN^- models are considered in the orthorhombic structure. In the orientationally disordered arrangement, the
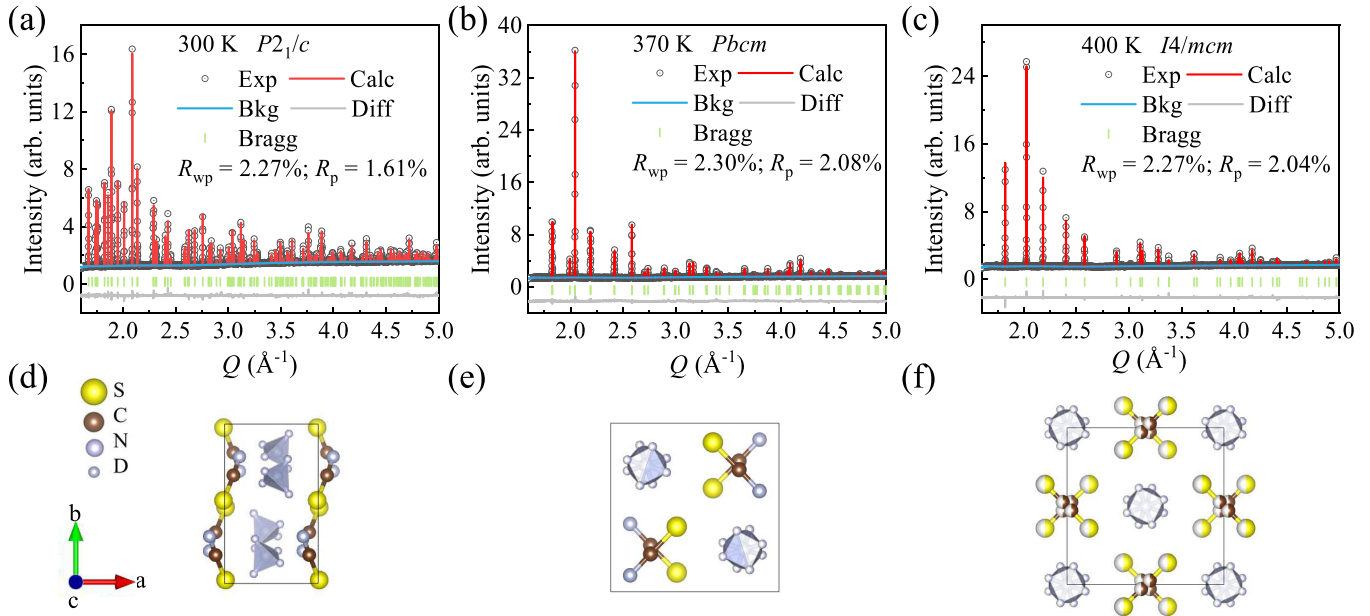
FIG. 1. (a)–(c) Rietveld refinements of diffraction spectra of ND_4SCN obtained at SuperHRPD at 300, 370, and 400 K, respectively. (d)–(f) The corresponding crystal structures of the monoclinic, orthorhombic, and tetragonal phases determined in the refinements.

fitting is not converged with reasonable refined parameters. In contrast, the fitting to the ordered model gives rise to a reasonable result. Therefore, the *Pbcm* model with disordered ND_4^+ and ordered SCN^- arrangements is adopted. The 400 K data are well fitted to the reported *I4/mcm* model with the simultaneous orientational disorder of NH_4^+ and SCN^-. The fitting is shown in Figs. 1(d)–1(f), and the full information regarding the crystal structures determined in the refinements is summarized in Table I. The ND_4^+ ions exhibit an orientationally disordered state with the occupation of deuterium atoms of 0.5 in the orthorhombic phase. The distribution formed by nitrogen and deuterium atoms shows a distorted, quasicubic trajectory, which is consistent with the dynamic motion of NH_4^+ given previously in our quasielastic neutron scattering results [11]. As a result, it can be understood that the entropy change of the colossal inverse BCE at the monoclinic to the orthorhombic phase transition is mainly contributed by the disorder of NH_4^+.

Figure 2(a) represents the diffraction spectra at all temperature points, where the detailed temperature dependence can be obtained. It is noticed that the monoclinic and orthorhombic phases coexist at 360 K. Applying the aforementioned structural models to corresponding phases, the refinements of the diffraction patterns yield the variation of lattice parameters with temperature, as shown in Fig. 2(b). In terms of coordination, a corresponds to $0.5c$, b corresponds to a, and c corresponds to $2b$. At the monoclinic-to-orthorhombic phase transition, the volume contraction ΔV_t is approximately 5%. The negative thermal expansion effect across a phase transition is intrinsically related to an inverse BCE in terms of Clausius-Clapeyron equation $dT_t/dP = \Delta V_t/\Delta S$, where T_t is the phase transition temperature [27–29]. Moreover, we can calculate the entropy change of the transition according to the volume change through this equation. The estimated

value is $126.7 \, \text{J} \, \text{kg}^{-1} \, \text{K}^{-1}$, which is almost the same as the experimental value.

B. Local atomic structures

As the orientational disorder of SCN^- is excluded in the average structure of the orthorhombic phase, we further examine this in the local structure using PDF analysis, which is defined as the probability of finding a pair of atoms at a specified interatomic distance r in the real space [30–32]. The total scattering spectra $S(Q)$ consist of both the Bragg diffraction peaks providing long-range order information and the diffuse scattering signal contributing to local disorder in disordered materials [33–34]. The normalized $S(Q)$ of the three phases are demonstrated in Fig. 3(a). The differences of $S(Q)$ of the monoclinic phase at 300 K and the orthorhombic phase at 380 K mainly reflect the fewer diffraction peaks caused by structural changes and the stronger diffuse scattering caused by the orientational disorder of ND_4^+ [Fig. 3(a), inset]. As for the tetragonal phase at 400 K, the intensity of the diffraction peaks continues to be reduced and the diffuse scattering becomes more pronounced due to the simultaneous orientational disorder of SCN^- and ND_4^+ in the tetragonal phase.

Figure 3(b) displays the derived $G(r)$ from the corresponding $S(Q)$. For the three phases, $G(r)$ at $r < 2 \, \text{Å}$ are quite similar, which are related to the intramolecular atomic pairs, whereas $G(r)$ at $r > 2 \, \text{Å}$ representing intermolecular atomic pairs are quite different. The $G(r)$ peaks at $r > 2 \, \text{Å}$ at 380 K and 400 K compared to those at 300 K are visibly shifted toward the lower distance, which is attributed to lattice contraction after the phase transition resulting in the closer distances between the intermolecular atoms, and the broadening indicates enhanced orientational disordering.

TABLE I. Full information on the crystal structures based on the refinements shown in Fig. 1.

Atoms	x	y	z	Occ	B (Å²)
$T = 300$ K, monoclinic, space group: $P2_1/c$					
$a = 4.236086(7)$ Å, $b = 7.148221(10)$ Å, $c = 13.009919(17)$ Å, $\beta = 97.77272(12)°$					
S	−0.0109(7)	0.9783(3)	0.19297(19)	1	1.32(7)
C	0.0951(2)	0.82122(16)	0.11560(9)	1	1.07(3)
N1	0.15960(19)	0.70440(12)	0.05911(6)	1	2.30(3)
N2	0.4430(3)	0.32719(19)	0.11207(9)	1	2.80(4)
D1	0.5702(4)	0.2958(2)	0.05632(13)	1	4.82(5)
D2	0.5931(4)	0.3716(2)	0.17262(13)	1	4.64(5)
D3	0.3248(4)	0.2202(3)	0.13305(12)	1	5.03(5)
D4	0.3118(5)	0.4397(2)	0.08967(13)	1	5.14(5)
$T = 370$ K, orthorhombic, space group: *Pbcm*					
$a = 6.887915(9)$ Å, $b = 6.868580(9)$ Å, $c = 7.937038(10)$ Å					
S	0.3927(4)	0.1141(4)	0.25	1	1.11(7)
C	0.2370(3)	0.2758(2)	0.25	1	2.58(4)
N1	0.11584(19)	0.40251(19)	0.25	1	4.36(5)
N2	0.7909(3)	0.25	0	1	3.92(4)
D1	0.7508(5)	0.3606(5)	0.0684(4)	0.5	6.88(9)
D2	0.9008(6)	0.2173(5)	−0.0841(4)	0.5	7.37(10)
D3	0.8260(5)	0.1308(6)	0.0767(5)	0.5	7.21(9)
D4	0.6682(6)	0.2914(8)	−0.0516(6)	0.5	9.27(15)
$T = 400$ K, tetragonal, space group: *I4/mcm*					
$a = 6.893863(6)$ Å, $b = 6.893863(6)$ Å, $c = 8.040935(11)$ Å					
S	0.640(2)	0.140(2)	0	0.5	2.1(4)
C	0.4724(3)	−0.0276(3)	0	0.5	1.99(6)
N1	0.3542(8)	−0.1458(8)	0	0.5	5.3(2)
N2	0	0	0.25	1	5.24(5)
D	0.11673(18)	−0.0420(3)	0.18296(15)	0.5	8.78(8)
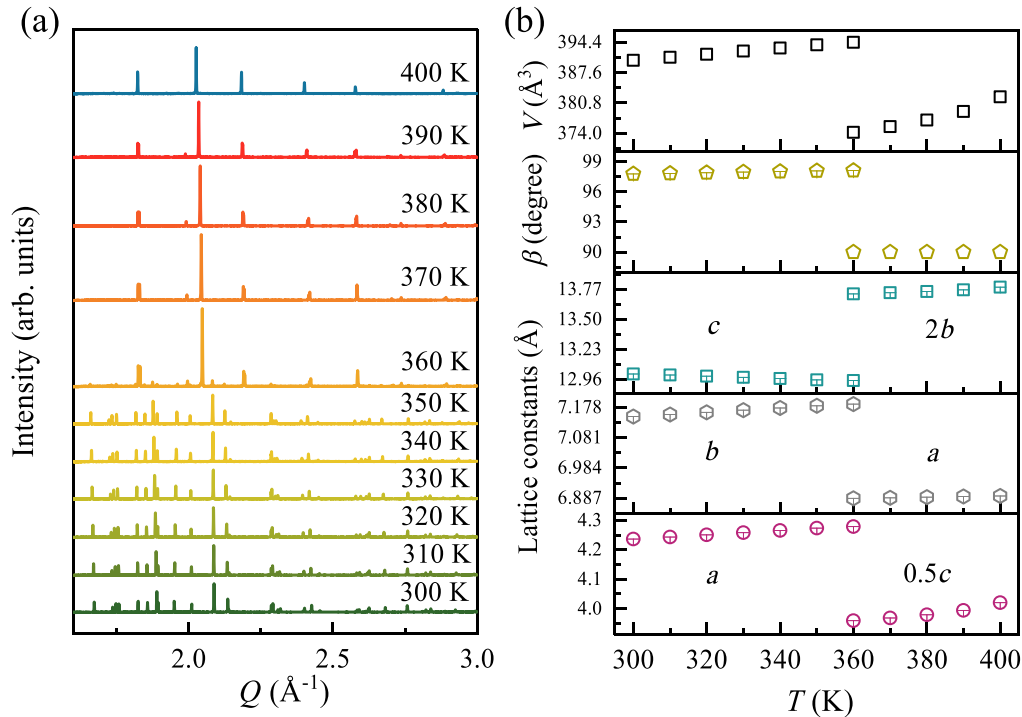
FIG. 2. (a) High-resolution neutron powder diffraction patterns of ND₄SCN across the two phase transitions. (b) Temperature dependence of the lattice dimensions determined in the refinements.
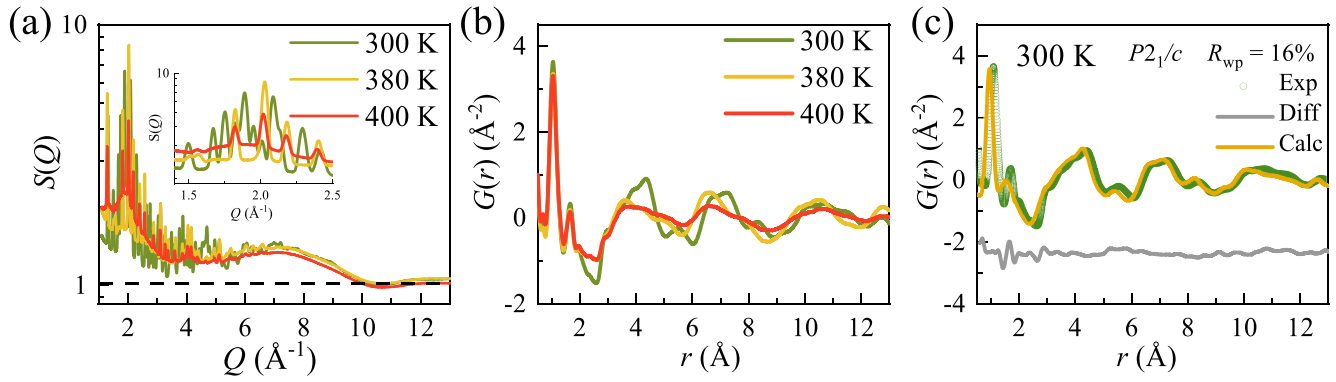
FIG. 3. (a) The normalized $S(Q)$ of ND_4SCN at different temperatures collected from the MPI of the CSNS, corresponding to the three phases. (b) The PDF curves obtained from the Fourier transform of the normalized $S(Q)$. (c) $G(r)$ at 300 K fitted to the monoclinic crystal structure model ($P2_1/c$).

The experimental $G(r)$ of 300 K is fitted to the crystal model of $P2_1/c$, as shown in Fig. 3(c), indicative of the nature of disorder free. The fitting difference is mainly located at $r \sim 1.6$ Å, which is contributed by C-S atomic pairs in the SCN^- ions. The significant fit residual may be caused by the deviation of the atomic distance of these two atoms. Furthermore, to identify the contribution of specific atom pairs to the total $G(r)$, partial $G(r)$ [as shown in Fig. 4(a)] are calculated based on the $P2_1/c$ model. Partial $G(r)$ of the N-N, N-S, N-C, D-C, and N-D atomic pairs are shown up to 13 Å. In the crystal structure of the monoclinic phase, the distances of N-D in ND_4^+ ions are ~ 0.95 Å. Therefore, the peak centered at ~ 0.9 Å is attributed to the N-D atomic pair, which contributes to the main intensity of the first peak in the experimental $G(r)$. Since the configuration of the ND_4^+ ion is almost rigid, the intensity and the peak position of the first peak are almost the same for different phases.

Then we focus on the region of $3.9 < r < 4.3$ Å, where $G(r)$ of the orthorhombic and tetragonal phases are the same, but significantly weaker than that of the monoclinic phase. Such a discrepancy can be well understood in the simulated partial $G(r)$. In this region, N-N, N-C, and D-C pairs are involved [the left blue shaded area in Fig. 4(a)]). At $r \sim 3.9$ Å, the main contributions are from the N-C atom pairs. The coordination between nitrogen and carbon atoms is plotted in Fig. 4(b) based on the crystal structure of $P2_1/c$. The N-C atomic pairs around 3.9 Å involve both the carbon atom and the nitrogen atom in ND_4^+, as well as the nitrogen atom in SCN^-. However, most of the intensity of the N-C partial $G(r)$ at 3.9 Å comes from the former. As shown in Fig. 4(a), the intensity of the peak at 4.3 Å is mainly from the N-N and D-C pairs, and the intensity of the latter is stronger than that of the former. The D-C coordination is given in Fig. 4(c). The D-C atom pair at 4.3 Å is related to the carbon atom in the SCN^- and the deuterium atoms away from the SCN^- in the surrounding ND_4^+. Accordingly, the suppressed intensity of the experimental $G(r)$ at 380 K and 400 K at $r \sim 4.3$ Å is ascribed to the D-C atomic pair. Thus, the changes in the correlations at $3.9 < r < 4.3$ Å can be attributed to the orientational disorder of ND_4^+ ions. A similar situation occurs at $r \sim 7.3$ Å, where the discrepancy between data at 300 K and

380 K mostly results from the reduction in the intensity of the D-C atomic pair due to the orientational disorder of ND_4^+.

In addition, we can see that there is also a difference in intensity between 380 K and 400 K around distance r from 6.4 to 7.0 Å [the right blue shaded area in Fig. 4(a)], with the intensity of 400 K being significantly lower than that of 380 K. Here we attribute it to the flip motion of SCN^-, given that the partial $G(r)$ at the range of 6.4 to 7.0 Å is mainly associated with the contribution of N-S, N-C, and N-N atomic pairs, as shown in Fig. 4(d). Moreover, the discrepancies between experimental $G(r)$ at 380 K and 400 K are not only limited to $r \sim 6.8$ Å, but also are exhibited at other positions at higher r. The apparent differences in experimental $G(r)$ between the orthorhombic and tetragonal phases indicate that the local structures of the two phases are not entirely identical. This also supports the neutron powder diffraction result that SCN^- ions are orientationally ordered in the orthorhombic phase and disordered in the tetragonal phase.

C. Lattice dynamics

After the average and local structures are well determined, we move to atomic vibrations. Raman scattering is an effective tool for demonstrating structural phase transitions and has already been used in the exploration of ordered-to-disordered phase transitions [35–40]. From the temperature-dependent Raman spectra measured at ambient pressure [Fig. 5(a)], the phase transition starts at 360 K and shows a two-phase coexistence region that is consistent with the results of temperature-dependent neutron diffraction. Above 360 K, multiple scattering peaks of the monoclinic phase are merged into three broadened peaks, indicating the creation of the orthorhombic phase.

From the spectrum measured at ambient conditions, several peaks are identified at 47 (P_1), 55 (P_2), 66 (P_3), 82 (P_4), 90 (P_5), 103 (P_6), 159 (P_7), and 175 (P_8) cm^{-1}, as shown in Fig. 5(b). Three small peaks at 47, 55, and 66 cm^{-1} are overlapped, representing the librational modes of SCN^-. The next three peaks at 82, 90, and 103 cm^{-1} are the signal of translational modes of SCN^-. They are followed by two weaker peaks located at 159 and 175 cm^{-1}, mainly related
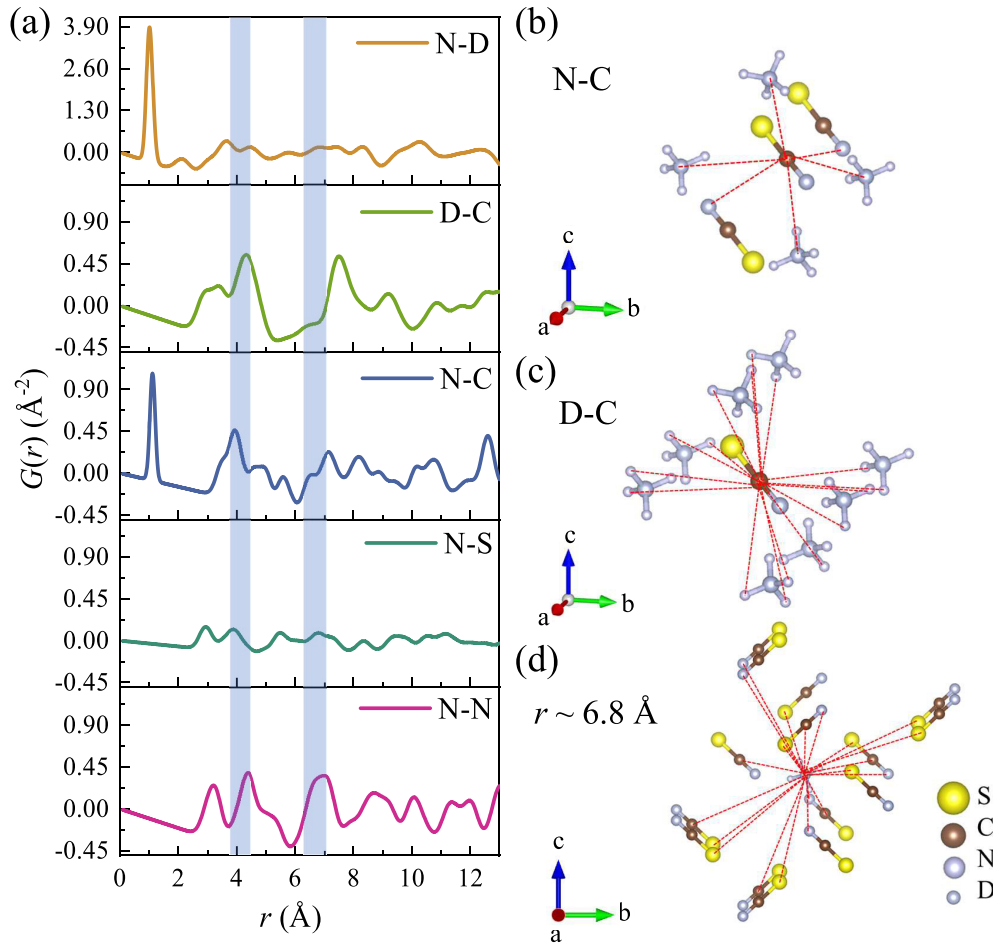
FIG. 4. (a). Partial $G(r)$ of N-N, N-S, N-C, N-D, and D-C atomic pairs based on the monoclinic crystal structure. The blue shaded areas corresponded to 3.9 to 4.3 and 6.4 to 7.0 Å. (b) N-C coordination around the carbon atom at $r \sim 3.9$ Å. (c) D-C coordination around the carbon atom at $r \sim 4.3$ Å. (d) Coordination at $r \sim 6.8$ Å around the center of the nitrogen atom in ND_4^+ ions.

to the translational modes of NH_4^+ [9,41]. With the temperature increasing, the relative intensities of the peaks at 47 and 55 cm^{-1} change significantly, where the former becomes stronger, whereas other peaks are too broadened to be distinguished.

At room temperature, the monoclinic-to-orthorhombic phase transition is induced by pressure, as shown in Fig. 5(c). Compared with the overbroadened Raman peaks of the orthorhombic phase at 370 K under ambient pressure, the peaks of the pressure-induced orthorhombic phase at room temperature are much clearer, where three obvious peaks are observed. An obvious change can be seen at 220 MPa, as shown in Fig. 5(d), where the multiple peaks of the librational modes of SCN$^-$ and the translational modes of SCN$^-$ transform into two broadened peaks centered at 62 and 117 cm^{-1}, respectively. The peaks of the translational modes of NH_4^+ become a shoulder adjacent to the translational modes of SCN$^-$. This phenomenon differs from previously reported studies, where the translational modes of NH_4^+ disappeared after the phase transition [9].

To investigate further the response of the lattice dynamics to temperature and pressure, we summarize the dependences

of the peak position on temperature and pressure, respectively. From the temperature dependence of the peak position in Fig. 5(e), one can observe a temperature-induced shift of the peaks toward the lower frequencies. A sudden discontinuity occurs at 360 K, indicative of the nature of the first-order phase transition. We estimate the average frequencies of the three modes for the ordered phase, represented by open red symbols in Fig. 5(e). The translational mode of NH_4^+ is softened at the phase transition, while both the librational and translational modes of SCN$^-$ show an abrupt hardening. As for the pressure effect, as shown in Fig. 5(f), a pronounced hardening behavior is observed for the librational and translational modes of SCN$^-$ at 220 MPa, while there is only a sizeable change for the translational mode of NH_4^+. In fact, the hardening is much stronger for the translational modes of SCN$^-$. As far as the phase transition mechanism of NH_4SCN is concerned, we suggest that excited transverse vibrations of SCN$^-$ ions during the phase transition result in the breakage of the hydrogen bonds between SCN$^-$ and NH_4^+ ions, which in turn leads to the orientation of NH_4^+ and the tilting of SCN$^-$ in the weakening of bonding [11]. Such a scenario is well supported by the pressure-enhanced librational and
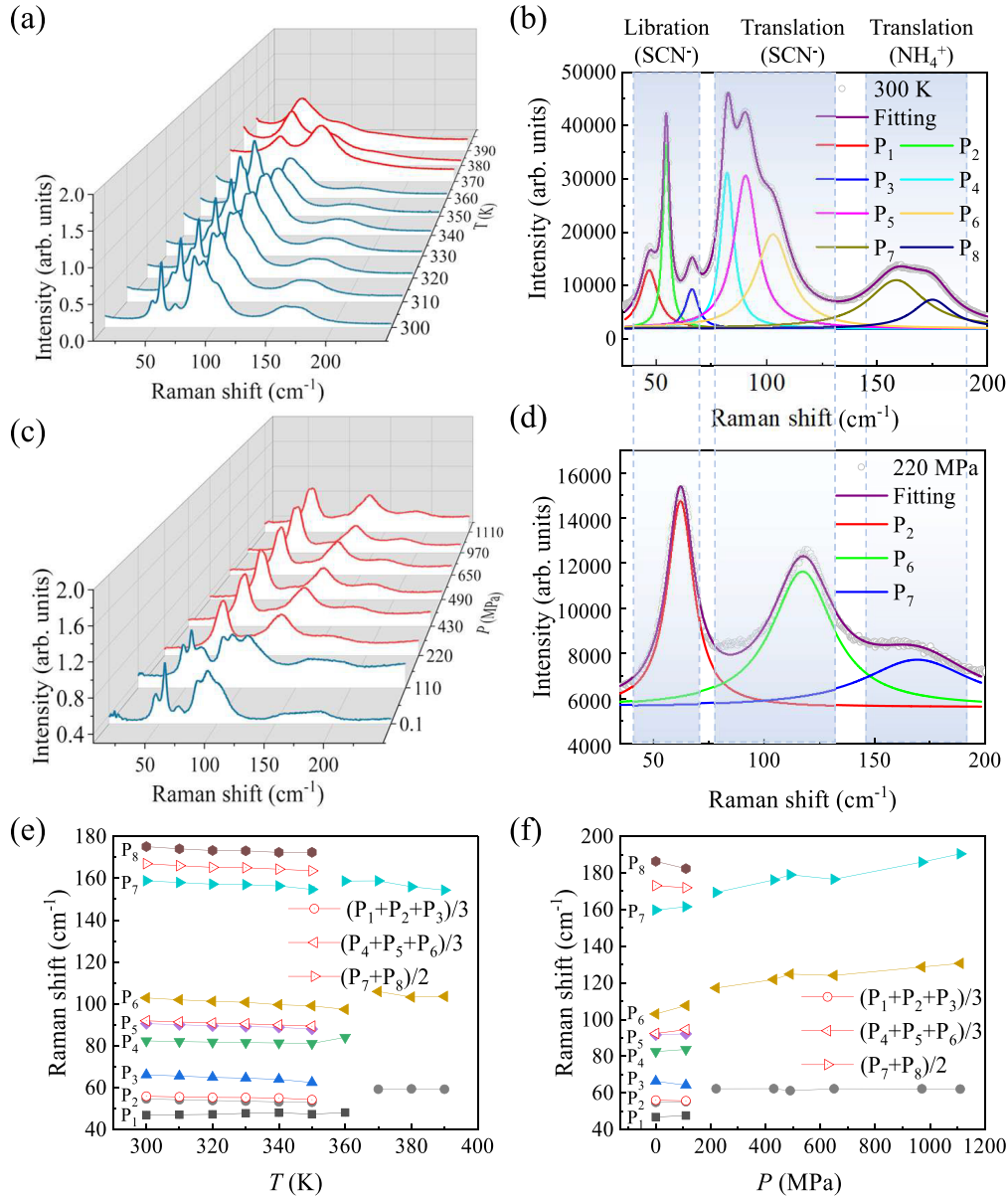
FIG. 5. (a) and (c) Variable temperature and pressure Raman scattering spectra of NH_4SCN, respectively. (b) and (d) Multiple-peak fitting of Raman spectra at 300 K under ambient pressure and 220 MPa, respectively, corresponding to the monoclinic and orthorhombic phases. The separated peaks are labeled with P_1 to P_8. (e) and (f) Peak positions varying with temperature and pressure, respectively.

translational modes of SCN^- observed here, considering that the transverse vibrations of SCN^- can be decomposed into these two modes.

IV. CONCLUSION

To summarize, we have precisely determined the average and local atomic structures of the three phases of NH_4SCN, using high-resolution neutron diffraction and neutron PDF analysis. The states of the ions in each phase are given: NH_4^+ and SCN^- ions are completely ordered in the low-temperature monoclinic phase; NH_4^+ ions are orientationally disordered in the medium-temperature orthorhombic phase with ordered SCN^- ions; both NH_4^+ and SCN^- show disordered states in the high-temperature tetragonal phase. Temperature- and

pressure-induced blue shifts of the vibrational frequency are observed for librational and translational modes of SCN^- at the monoclinic-to-orthorhombic phase transition. The enhanced librational and translational modes of SCN^- weaken the linkage of hydrogen bond networking and ultimately facilitate the phase transition to the orthorhombic phase.

[1] B. Li *et al.*, Colossal barocaloric effects in plastic crystals, Nature **567**, 506 (2019).

[2] P. Lloveras, A. Aznar, M. Barrio, P. Negrier, C. Popescu, A. Planes, L. Mañosa, E. Stern-Taulats, A. Avramenko, N. D. Mathur, X. Moya, and J.- L. Tamarit, Colossal barocaloric effects near room temperature in plastic crystals of neopentyl-glycol, Nat. Commun. **10**, 1803 (2019).

[3] A. Aznar, P. Lloveras, M. Barrio, P. Negrier, A. Planes, L. Mañosa, N. D. Mathur, X. Moya, and J.-L. Tamarit, Reversible and irreversible colossal barocaloric effects in plastic crystals, J. Mater. Chem. A. **8**, 639 (2020).

[4] A. Aznar, P. Negrier, A. Planes, L. Mañosa, E. Stern-Taulats, X. Moya, M. Barrio, J.- L. Tamarit, and P. Lloveras, Reversible colossal barocaloric effects near room temperature in 1-*X*-adamantane ($X =$ Cl, Br) plastic crystals, Appl. Mater. Today **23**, 101023 (2021).

[5] K. Zhang, R. Song, J. Qi, Z. Zhang, Z. Zhang, C. Yu, K. Li, Z. Zhang, and B. Li, Colossal barocaloric effect in carboranes as a performance tradeoff, Adv. Funct. Mater. **32**, 2112622 (2022).

[6] J. Li, D. Dunstan, X. Lou, A. Planes, L. Mañosa, M. Barrio, J.-L. Tamarit, and P. Lloveras, Reversible barocaloric effects over a large temperature span in fullerite C_{60}, J. Mater. Chem. A. **8**, 20354 (2020).

[7] J. Timmermans, Plastic crystals: A historical review, J. Phys. Chem. Solids **18**, 1 (1961).

[8] D. Chandra, W. Ding, and R. A. Lynch, Phase transitions in "plastic crystals," J. Less Common Met. **168**, 159 (1991).

[9] G. Burns, F. H. Dacol, and B. Welber, Lattice vibrational study of the phase transition in the plastic crystal adamantane ($C_{10}H_{16}$), Solid State Commun. **32**, 151 (1979).

[10] T. Hayasaki, S. Hirakawa, and H. Honda, New ionic plastic crystals of NR_4BEt$_3$Me ($R =$ Me and Et) and N$R_x R'_{4-x}$BEt$_3$Me ($R =$ Et, $R' =$ Me and Pr, $x = 1$–3) in a new class of plastic crystals, Bull. Chem. Soc. Jpn. **86**, 993 (2013).

[11] Z. Zhang *et al.*, Thermal batteries based on inverse barocaloric effects, Sci. Adv. **9**, eadd0374 (2023).

[12] L. S. Smirnov, D. Smith, I. Natkaniec, and V. B. Zlokazov, *Neutron spectroscopy of the librational mode ammonium ions in the monoclinic phase of* NH_4SCN (Institute for Theoretical and Experimental Physics, Moscow, 2002).

[13] L. S. Smirnov, V. A. Goncharova, E. L. Gromnitskaya, G. G. Il'ina, I. Natkaniec, A. I. Solov'ev, and O. V. Stal'gorova, The acoustic and neutron scattering investigations of NH_4SCN phase diagram, High Press. Res. **13**, 65 (1994).

[14] A. Hamada, S. Yamamoto, and Y. Shinnaka, Structural study of tetragonal-orthorhombic phase transition in NH_4SCN, J. Phys. Soc. Japan **59**, 954 (1990).

[15] J. W. Bats and P. Coppens, The experimental charge distribution in sulfur-containing molecules: A study of the deformation density in NH_4SCN at 81 K by combined x-ray and neutron diffraction, Acta Cryst. B **33**, 1542 (1977).

[16] Y. Kinsho, N. Onodera, M. Sakiyama, and S. Seki, Thermodynamic studies on phase transitions of potassium thiocyanate and ammonium thiocyanate crystals, Bull. Chem. Soc. Jpn. **52**, 395 (1979).

[17] R. Blinc, J. Seliger, V. Zagar, T. Apih, and J. Dolinsek, ^{14}N nuclear-quadrupole-resonance study of the structural phase transitions in NH_4SCN, Phys. Rev. B **42**, 8125 (1990).

[18] G. D. Tewari, D. P. Khandelwal, and H. D. Bist, Raman scattering study of phase transitions in NH_4SCN. J. Chem. Phys. **82**, 5624 (1985).

[19] S. Torii, M. Yonemura, T. Y. S. P. Putra, J. Zhang, P. Miao, T. Muroya, R. Tomiyasu, T. Morishima, S. Sato, H. Sagehashi, Y. Noda, and T. Kamiyama, Super high resolution powder diffractometer at J-PARC, J. Phys. Soc. Jpn. **80**, SB020 (2011).

[20] R. Oishi, M. Yonemura, Y. Nishimaki, S. Torii, A. Hoshikawa, T. Ishigaki, T. Morishima, K. Mori, and T. Kamiyama, Rietveld analysis software for J-PARC, Nucl. Instrum. Methods Phys. Res. **600**, 94 (2009).

[21] J. Xu, Y. Xia, Z. Li, H. Chen, X. Wang, Z. Sun, and W. Yin, Multi-physics instrument: Total scattering neutron time-of-flight diffractometer at China Spallation Neutron Source, Nucl. Instrum. Meth. A **1013**, 165642 (2021).

[22] O. Arnold *et al.*, Mantid: Data analysis and visualization package for neutron scattering and μSR experiments, Nucl. Inst. Methods Phys. Res. A **764** 156 (2014).

[23] C. L. Farrow, PDFfit2 and PDFgui: Computer program for studying nanostructure in crystals, J. Phys. Condens. Matter **19**, 335219 (2007).

[24] K. Momma and F. Izumi, VESTA 3 for three-dimensional visualization of crystal, volumetric and morphology data, J. Appl. Crystallogr. **44**, 1272 (2011).

[25] J. Walker, K. P. Marshall, J. Salgado-Beceiro, B. A. D. Williamson, N. S. Løndal, S. Castro-Garcia, M. S. Andujar, S. M. Selbach, D. Chernyshov, and M. A. Einarsrud, Mesophase transitions in $[(C_2H_5)_4N][FeBrCl_3]$ and $[(CH_3)_4N][FeBrCl_3]$ ferroic plastic crystals, Chem. Mater. **34**, 2585 (2022).

[26] E. Shalaev, K. Wu, S. Shamblin, J. F. Krzyzaniak, and M. Descamps, Crystalline mesophases: Structure, mobility, and pharmaceutical properties, Adv. Drug Deliv. Rev. **100**, 194 (2016).

[27] L. Mañosa, D. González-Alonso, A. Planes, M. Barrio, J. L. Tamarit, I. S. Titov, M. Acet, A. Bhattacharyya, and S. Majumdar, Inverse barocaloric effect in the giant magnetocaloric La–Fe–Si–Co compound, Nat Commun. **2**, 595 (2011).

[28] A. Aznar, P. Lloveras, J. Y. Kim, E. Stern-Taulats, M. Barrio, J. L. Tamarit, C. F. Sánchez-Valdés, J. L. S. Llamazares, N. D. Mathur, and X. Moya, Giant and reversible inverse barocaloric effects near room temperature in ferromagnetic MnCoGeB$_{0.03}$, Adv. Mater. **31**, 19035 (2019).

[29] E. Stern-Taulats, P. Lloveras, M. Barrio, E. Defay, M. Egilmez, A. Planes, J. L. Tamarit, L. Mañosa, N. D. Mathur, and X. Moya, Inverse barocaloric effects in ferroelectric $BaTiO_3$ ceramics, APL Mater. **4**, 091102 (2016).

[30] P. Bordet, Local structure studies using the pair distribution function, EPJ Web Conf. **104**, 01003 (2015).

[31] Th. Proffen, S. J. L. Billinge, T. Egami, and D. Louca, Structural analysis of complex materials using the atomic pair distribution function: A practical guide, Z. Kristallogr. **218**, 132 (2003).

[32] B. H. Toby and T. Egami, Accuracy of pair distribution function analysis applied to crystalline and non-crystalline materials, Acta Coest. **A48**, 336 (1992).

[33] M. T. Dove, M. G. Tucker, and D. A. Keen, Neutron total scattering method: Simultaneous determination of long-range and short-range order in disordered materials, Eur. J. Mineral. **14**, 331 (2002).

[34] M. W. Terban and S. J. L. Billinge, Structural analysis of molecular materials using the pair distribution function, Chem. Rev. **122**, 1208 (2022).

[35] J. F. Scott, Soft-mode spectroscopy: Experimental studies of structural phase transitions, Rev. Mod. Phys. **46**, 83 (1974).

[36] K. A. Müller and H. Thomas, *Structural Phase Transitions I*, (Springer, Berlin, 1981).

[37] W. H. Weber and R. Merlin, *Raman Scattering in Materials Science* (Springer, Berlin, 2000).

[38] A. B. Jain and S. K. Deb, Order-disorder transition in pentaerythritol using Raman scattering, Solid State Commun. **318**, 113964 (2020).

[39] C. Carabatos-Nedelec and P. Becker, Order–disorder and structural phase transitions in solid-state materials by scattering Raman analysis, J. Raman Spectrosc. **28**, 663 (1997).

[40] A. Hédoux, Y. Guinet, F. Capet, F. Affouard, and M Descamps, Raman effects under pressure in chloroadamantane plastic crystal, J. Phys. Condens. Matter **14** 8725 (2002).

[41] G. D. Tewari, G. S. Raghuvanshi, D. P. Khandelwal, and H. D. Bist, Study of structural phase transition in NH_4SCN from Raman scattering, Chem. Phys. Lett. **104**, 328 (1984).